Nanoscale metamaterial optical waveguides with ultrahigh refractive indices

Yingran He,[1,2] Sailing He,[2] Jie Gao,[1,3] and Xiaodong Yang[1,4]

[1]*Department of Mechanical and Aerospace Engineering, Missouri University of Science and Technology, Rolla, Missouri 65409, USA*

[2]*Centre for Optical and Electromagnetic Research, Zhejiang Provincial Key Laboratory for Sensing Technologies, Zhejiang University, Hangzhou 310058, China*

[3]*e-mail: gaojie@mst.edu*

[4]*e-mail: yangxia@mst.edu*

Received June 4, 2012; revised July 16, 2012; accepted August 1, 2012; posted August 1, 2012 (Doc. ID 169958); published August 29, 2012

We propose deep-subwavelength optical waveguides based on metal–dielectric multilayer indefinite metamaterials with ultrahigh effective refractive indices. Waveguide modes with different mode orders are systematically analyzed with numerical simulations based on both metal–dielectric multilayer structures and the effective medium approach. The dependences of waveguide mode indices, propagation lengths, and mode areas on different mode orders, free-space wavelengths, and sizes of waveguide cross sections are studied. Furthermore, waveguide modes are also illustrated with iso-frequency contours in the wave vector space in order to investigate the mechanism of waveguide mode cutoff for high-order modes. The deep-subwavelength optical waveguide with a size smaller than $\lambda_0/50$ and a mode area in the order of $10^{-4}\lambda_0^2$ is realized, and an ultrahigh effective refractive index up to 62.0 is achieved at the telecommunication wavelength. This new type of metamaterial optical waveguide opens up opportunities for various applications in enhanced light–matter interactions.

OCIS code: 160.3918, 230.7370, 250.5403, 310.6628.

The emergence of metamaterials with artificially engineered subwavelength composites offers a new perspective on light manipulation and exhibits intriguing optical phenomena such as negative refraction [1–3], subdiffraction imaging [4–6], invisible cloaking [7–9], and high index of refraction [10–12]. One unique kind of optical metamaterials is the indefinite metamaterial with extreme anisotropy, in which not all the principal components of the permittivity tensor have the same sign [13]. The nonmagnetic design and the off-resonance operation of the indefinite metamaterial can considerably reduce the optical absorption associated with conventional metamaterials [14]. The unique hyperbolic dispersion of the indefinite metamaterial enables the demonstration of negative refraction [15], subdiffraction optical imaging with hyperlenses [4–6], the strong enhancement of photonic density of states [16,17], slow-light waveguides [18–20], and broadband light absorbers [21]. Since the hyperbolic dispersion eliminates the cutoff of large wave vectors, the effective refractive index can be arbitrarily high. Such a capability is potentially important for building nanoscale optical cavities [22,23] and deep-subwavelength optical waveguides [24,25] with strong optical energy confinement. In reality, besides natural indefinite media such as graphite in the ultraviolet spectrum [26], an indefinite metamaterial is usually constructed with metal–dielectric multilayer structures [6] rather than a metallic nanowires array embedded in dielectrics [15] due to the difficulties of device fabrication.

Since optical waveguides play an important role in many fundamental studies of optical physics at nanoscale and in exciting applications in nanophotonics, optical waveguides based on indefinite metamaterials have been recently studied [19,20,24,27–30], in order to obtain novel optical properties beyond the conventional dielectric waveguides, especially slow-light propagation [19,20], surface mode guidance [29,30], and subwavelength mode compression [24,25]. In this paper, we propose deep-subwavelength optical waveguides based on metal–dielectric multilayer indefinite metamaterials, which support waveguide modes with tight photon confinement due to the ultralarge wave vectors inside indefinite metamaterials, and therefore ultrahigh effective refractive indices. The optical properties of waveguide modes will be presented with the mode analysis in both the real space and the wave vector space. The dependences of waveguide mode indices, propagation lengths, and mode areas on different mode orders, free-space wavelengths, and sizes of waveguide cross sections are investigated. The mechanism of waveguide mode cutoff is also illustrated in the wave vector space. This new type of metamaterial optical waveguide with ultrahigh refractive indices and extremely tight photon confinement will be of great importance in the enhancement of light–matter interactions, such as nanoscale lasers [31], quantum electrodynamics [32], nonlinear optics [33], optomechanics [34], and transformation optics [35].

Figure 1(a) shows the schematic of optical waveguides based on metal–dielectric multilayer indefinite metamaterials. The multilayer metamaterial is constructed with alternative layers of silver (Ag) and germanium (Ge). Each period includes a 4 nm silver layer and a 6 nm germanium layer, leading to a multilayer structure with period $a = 10$ nm and filling ratio of silver $f_m = 0.4$. Since the period of the multilayer a is much less than the operation wavelength ($a \ll 2\pi/k$, where k is wave vector), the multilayer metamaterial can be treated as

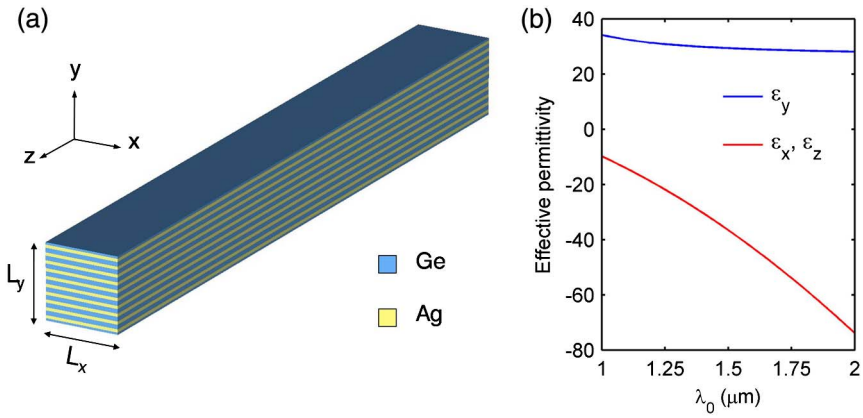

Fig. 1. (Color online) (a) Schematic of a nanoscale optical waveguide made of the metal–dielectric multilayer indefinite metamaterial, which is constructed with alternative layers of 4 nm silver and 6 nm germanium. Nanoscale optical waveguides can be created due to the TIR at the metamaterial-air interface. (b) Principal components of the permittivity tensor for the multilayer metamaterial with a silver filling ratio of $f_m = 0.4$, calculated from the effective medium theory (Eq. 1), where ε_y is positive and ε_z (ε_x) is negative. For example, $\varepsilon_x = \varepsilon_z = -39.8 + 2.1i$ and $\varepsilon_y = 29.2 + 0.1i$ at $\lambda_0 = 1.55$ μm.

a homogeneous effective medium and the principle components of the anisotropic permittivity tensor can be determined from the Maxwell–Garnet theory [36,37],

$$\varepsilon_x = \varepsilon_z = f_m\varepsilon_m + (1-f_m)\varepsilon_d, \varepsilon_y = \frac{\varepsilon_m\varepsilon_d}{f_m\varepsilon_d + (1-f_m)\varepsilon_m}, \quad (1)$$

where f_m is the volume filling ratio of silver, and ε_d and ε_m are the permittivity corresponding to germanium and silver, respectively. The permittivity of germanium is $\varepsilon_d = 16$, and the optical properties of silver are described by the Drude model $\varepsilon_m(\omega) = \varepsilon_\infty - \omega_p^2/(\omega^2 - i\omega\gamma)$, with a background dielectric constant $\varepsilon_\infty = 5$, plasma frequency $\omega_p = 1.38\times 10^{16}$ rad/s, and collision frequency $\gamma = 5.07\times 10^{13}$ rad/s [38]. Figure 1(b) shows the calculated effective permittivity tensor for the multilayer metamaterial with a silver filling ratio of $f_m = 0.4$ for the free-space wavelength λ_0 ranging from 1 to 2 μm. The permittivity shows negative value along x and z directions (parallel to the multilayers) and positive value along y direction (vertical to the multilayers). Since large wave vectors are supported in indefinite metamaterials due to the hyperbolic dispersion, ultrahigh refractive indices can be reached, which will enable the formation of optical waveguides with deep-subwavelength cross sections based on the total internal reflection (TIR) at the interface between metamaterial and air, as illustrated in Fig. 1(a).

Figure 2 plots the waveguide mode profiles of different mode orders supported in a metamaterial waveguide with a cross section of $L_x = L_y = 100$ nm at free-space wavelength $\lambda_0 = 1$ μm, calculated from the finite-element method (FEM) software package (COMSOL). The distributions of optical field components H_x, E_y, and electromagnetic (EM) energy density W for different modes calculated from the multilayer structure are shown in Figs. 2(a), 2(c), and 2(d). It is clear that these waveguide modes with different mode orders (m_x, m_y) exhibit spatial oscillations in both x and y directions, with specified wave vectors k_x and k_y, in addition to the propagation wave vector k_z along the waveguide. For the mode order (m_x, m_y), m_x and m_y represent the number of peaks in H_x profile inside the waveguide along the x direction and the y direction, respectively. Compared with the H_x components, the E_y components show exactly the same number of peaks within the waveguide. However, the W profile is related to the mode order (m_x, m_y) in a different way, and its maximums approximately occur at locations where H_x and E_y have the largest spatial gradients. The EM energy density W is calculated by taking the strongly dispersive property of silver into account, as $W(x,y) = \frac{1}{2}\,\mathrm{Re}[\frac{d(\omega\varepsilon_m)}{d\omega}]\varepsilon_0|\vec{E}|^2 + \frac{1}{2}\mu_0|\vec{H}|^2$. Figure 2(b) gives the distributions of optical field components for $(1, m_y)$ mode calculated with the effective medium method, which agree very well with the multilayer results in Fig. 2(a).

In order to study the optical properties of these waveguide modes with different mode orders in the waveguide with a cross section of $L_x = L_y = 100$ nm, waveguide mode indices along the propagation direction $n_{\mathrm{eff},z}$, propagation lengths L_m and mode areas A_m as functions of free-space wavelength λ_0 are shown in Fig. 3. As indicated from Fig. 3(a), waveguide modes with a lower m_x or a higher m_y tend to have larger mode indices $n_{\mathrm{eff},z}(= k_z/k_0)$ at a specific wavelength λ_0. As a result, the mode index of the (1, 1) mode is the largest in the $(m_x, 1)$ mode group and the smallest in the $(1, m_y)$ mode group. It is clear that waveguide mode indices will decrease as the wavelength λ_0 grows, which is caused by the material dispersion shown in Fig. 1(b), but the decrease rates depend on different mode orders m_x. Waveguide mode with a higher mode order m_x along the x direction will have a faster index decrease rate due to the larger k_x and the stronger effect from the material dispersion, which will eventually result in the waveguide mode cutoff ($n_{\mathrm{eff},z} < 1$) at a lower wavelength. In contrast to the $(3, m_y)$ and $(2, m_y)$ modes, the $(1, m_y)$ modes do not have mode cutoff due to the zero wave vector along the x direction ($k_x = 0$). The propagation lengths calculated from $L_m \equiv 1/2\,\mathrm{Im}(k_z) = \lambda_0/4\pi\,\mathrm{Im}(n_{\mathrm{eff},z})$ are plotted in Fig. 3(b). When the wavelength is much lower than the mode cutoff wavelength, higher-order modes for a given wavelength have shorter propagation lengths, since high-order modes have tight mode confinement with large refractive indices in the propagation direction and small mode areas in the transverse direction, which will induce large absorption losses. As an example, for the (2, 1) mode, as the wavelength increases, the propagation length will go up first, due to the reduced absorption loss in the material dispersion. When the wavelength gets

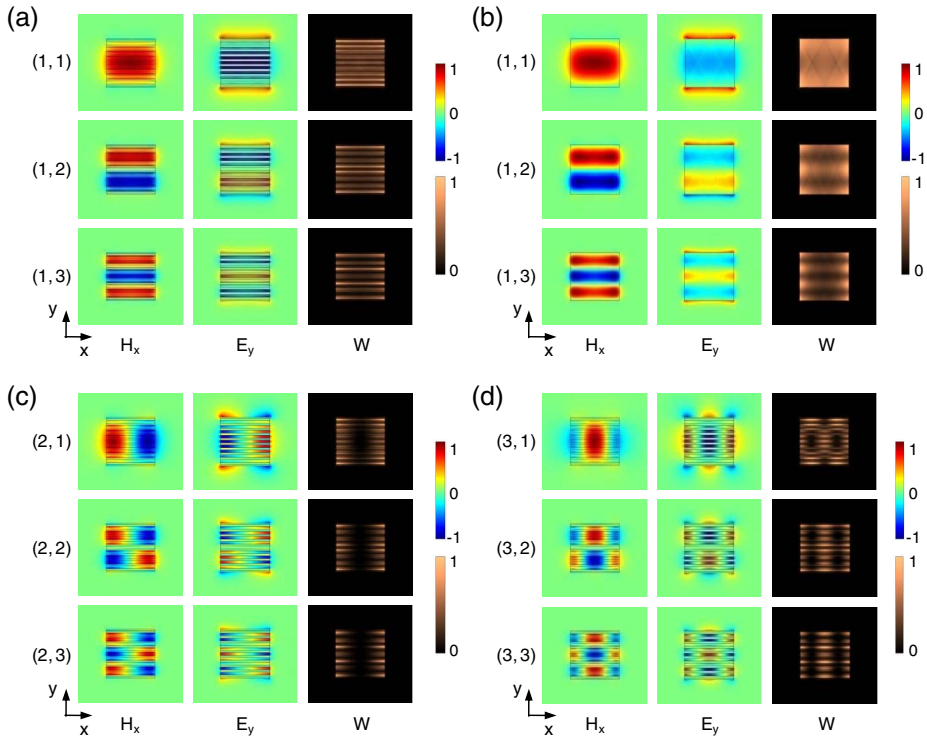

Fig. 2. (Color online) Distributions of magnetic field H_x, electric field E_y, and EM energy density W for waveguide modes with different mode orders supported in the metamaterial waveguide with cross section of 100 by 100 nm at $\lambda_0 = 1$ μm. Waveguide modes with mode orders of $(1, m_y)$, $(2, m_y)$, and $(3, m_y)$ in metal–dielectric multilayer waveguide structures are shown in (a), (c), and (d), respectively. The $(1, m_y)$ modes are also calculated with the effective medium method, as shown in (b), which agree very well with the multilayer results in (a).

close to the mode cutoff wavelength, the propagation length will drop dramatically, due to the increased radiation leakage of the waveguide mode confined by TIR. The observed behavior of the propagation length results from the tradeoff between the absorption loss and the mode radiation loss. The $(1, m_y)$ modes maintain long propagation lengths since there is no mode cutoff. The (1, 1) mode turns out to have the longest propagation length, which is around 700 nm at $\lambda_0 = 1.55$ μm. This subwavelength propagation length in fact covers several operation wavelengths inside the waveguide with a high mode index of 8.3 at $\lambda_0 = 1.55$ μm. Figure 3(c) gives the calculated mode areas A_m for all the waveguide modes, where $A_m \equiv \frac{\iint W(x,y)\mathrm{d}x\mathrm{d}y}{\max[W(x,y)]}$. The results show that the metamaterial waveguides give deep-subwavelength optical energy confinement with the mode areas down to the order of 10^{-3} (λ_0^2). Since strong optical field component E_z can be induced at the waveguide boundaries due to the tight confinement of optical modes, the location of EM energy density maximum will vary from the waveguide boundaries to the interior region as the optical wavelength changes, leading to some peculiar variation behaviors of the plotted mode areas in Fig. 3(c). It should be noted that the collision frequency of silver film with nanoscale confinement will increase compared with the collision frequency of bulk silver [39], which will induce more optical losses and thus decrease the propagation length. However, the ultrahigh refractive indices can still be maintained since the hyperbolic dispersion of the metamaterial always exists, and therefore the optical mode confinement is almost the same.

Since the multilayer metamaterial can be treated as an indefinite medium with the principle components of permittivity tensor calculated in Eq. (1), the dispersion relation for such uniaxial anisotropic material is [22]

$$\frac{k_x^2 + k_z^2}{\varepsilon_y} + \frac{k_y^2}{\varepsilon_z} = k_0^2, \tag{2}$$

where k_0 is the free-space wave vector corresponding to the free-space wavelength λ_0. The components of effective refractive index n_{eff} are related to wave vector components along different directions, as $(n_{\mathrm{eff},x}, n_{\mathrm{eff},y}, n_{\mathrm{eff},z}) = (k_x/k_0, k_y/k_0, k_z/k_0)$. The three-dimensional (3D) hyperboloid iso-frequency contour (IFC) of indefinite metamaterial in k-space for a specific λ_0 is shown in Fig. 4(a), where the wave vector component along the propagation direction k_z can be obtained from Eq. (2) if the other two components k_x and k_y are known for a specific mode order (m_x, m_y). As shown in Fig. 2, the H_x field distributions show harmonic oscillations with a cosine function along the x direction and a sine function along the y direction, due to the extreme anisotropy of the indefinite metamaterial and therefore different boundary conditions on the waveguide interfaces. For the (1, 1) mode, the field profile shows a zero phase accumulation (a constant phase) along the x direction, and a π phase accumulation along the y direction. In general, for a specific (m_x, m_y) mode, H_x will undergo a phase accumulation of $(m_x - 1)\pi$ along the x direction and a phase accumulation of $m_y\pi$ along the y direction. The values of k_x and k_y are then related to the size of the waveguide cross section and the mode order,

$$k_x = (m_x - 1)\frac{\pi}{L_x}, k_y = m_y\frac{\pi}{L_y}, \tag{3}$$

with $m_x = 1, 2, 3$ and $m_y = 1, 2, 3$ for the waveguide modes shown in Fig. 2. Strictly speaking, the evanescent field outside

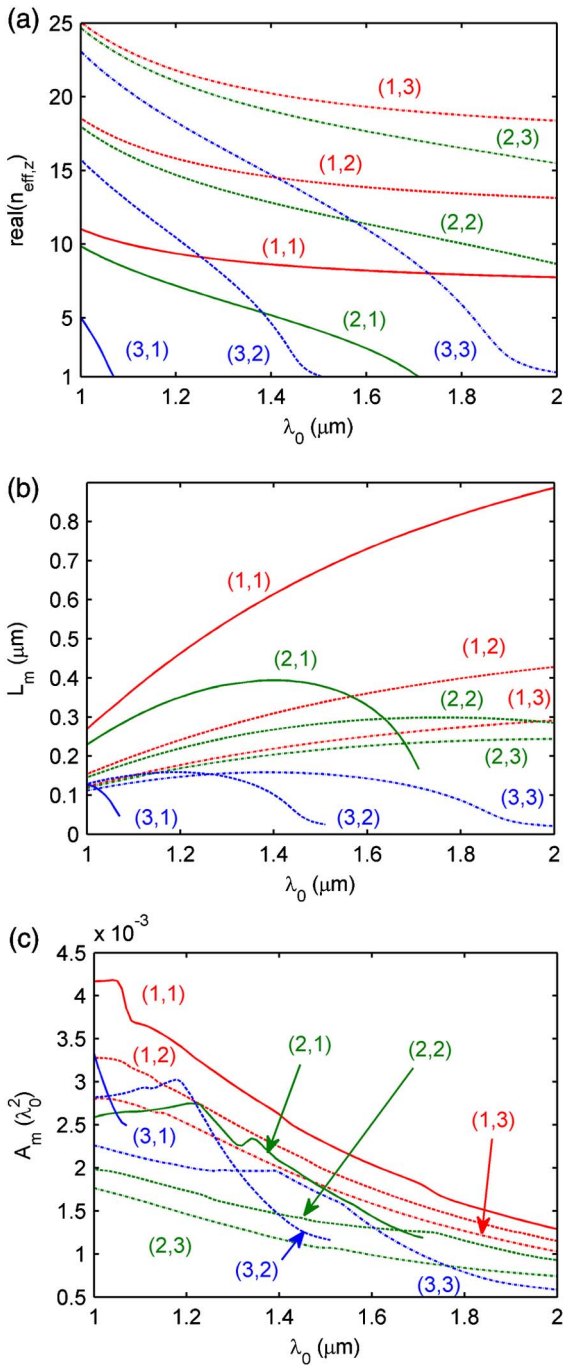

Fig. 3. (Color online) Dependences of (a) waveguide mode indices along the propagation direction $n_{\mathrm{eff},z}$; (b) propagation lengths L_m, and (c) mode areas A_m on wavelength λ_0 for waveguide modes with different mode orders in the waveguide with cross section of 100 by 100 nm. All the $(3, m_y)$ modes and the (2, 1) mode have mode cutoff at certain wavelengths. The propagation lengths depend on both the absorption loss and the mode radiation loss. The mode areas are on the order of 10^{-3} (λ_0^2), due to the tight photon confinement of waveguide modes.

the waveguide will result in a nonzero reflection phase change at the waveguide boundaries due to the TIR [40], which will contribute to the round-trip phase accumulation along the transverse direction of the waveguide. In the derivation of Eq. (3), however, the effect of evanescent field outside the waveguide has been neglected since its magnitude is much weaker than the optical field confined within the waveguides. Based on the values of the wave vector components, a waveguide mode can be mapped on the hyperboloid surface in the 3D k-space. If there are common crossing points between two perpendicular cutting planes as defined in Eq. (3) and the 3D hyperboloid surface, the waveguide mode with a mode order of (m_x, m_y) will exist. Next, waveguide modes with different mode orders will be illustrated with IFCs in the k-space in order to investigate the mechanism of waveguide mode cutoff for high-order modes.

In Fig. 4, waveguide modes supported in the waveguide with fixed size of $L_x = 100$ nm and $L_y = 100$ nm are analyzed in k-space. Figure 4(a) shows the hyperboloid IFC for a specific wavelength λ_0, together with two cutting planes in gray color at $k_x = 0$ and $k_x/k_0 = \lambda_0/L_x$, which represent mode orders of $m_x = 1$ and $m_x = 3$, respectively. The crossing curves between the two cutting planes and the hyperboloid IFC surface are plotted in Figs. 4(b) and 4(c), respectively, at different wavelengths of $\lambda_0 = 1$ μm (blue color) and $\lambda_0 = 1.55$ μm (red color). These hyperbolic curves are calculated from the effective medium method. The shapes of the curves will change as the wavelength varies, due to the permittivity dispersion of the indefinite metamaterial at different frequencies. The markers in Figs. 4(b) and 4(c) represent the $(1, m_y)$ and $(3, m_y)$ modes calculated from multilayer metamaterial waveguide structures, which locate on the IFCs showing that the effective medium approximation is valid in this situation. It is noted that the hyperbolic curves have changed their opening directions from the z direction in Fig. 4(b) to the y direction in Fig. 4(c). According to Fig. 4(b), there are no mode cutoffs for the $(1, m_y)$ modes. However, the (3, 1) and (3, 2) modes have cutoff at $\lambda_0 = 1.55$ μm in Fig. 4(c), since k_z is not available for the given mode orders. For $\lambda_0 = 1$ μm, the dispersion curve has much lower k_y, so that all the $(3, m_y)$ modes still exist.

The effects of waveguide cross sections on the mode cutoff are then studied at a fixed wavelength of $\lambda_0 = 1.55$ μm. By varying the waveguide height L_y or the waveguide width L_x, wave vectors will change based on Eq. (3), so that the corresponding cutting planes will also shift. Figure 5 illustrates the waveguide modes in k-space for two waveguides with the same width $L_x = 100$ nm but different heights, $L_y = 80$ nm and $L_y = 150$ nm, respectively. In Fig. 5(a), three cutting planes corresponding to $m_x = 1$, 2, and 3 for the fixed L_x are drawn in red, green, and blue, respectively. The crossing curves between these cutting planes and the hyperboloid IFC surface are plotted in Figs. 5(b) and 5(c) for different waveguide heights, which are calculated from the effective medium method. It is noted that the hyperbolic curves with $m_x = 1$ open towards the z direction, while the hyperbolic curves with $m_x = 2$ and $m_x = 3$ open towards the y direction. The markers in Figs. 5(b) and 5(c) represent the (m_x, m_y) modes calculated from multilayer metamaterial waveguide structures. All the $(1, m_y)$ modes located on a hyperbolic curve with z-direction opening do not have mode cutoff since there is always a corresponding k_z, no matter what the value of k_y is. However, as shown in Fig. 5(b), the (3, 1) mode has cutoff for $L_y = 80$ nm since k_z is not available for the given mode order. In Fig. 5(c), all the $(3, m_y)$ modes and the (2, 1) mode have cutoff due to the reduced k_y value as L_y gets larger. Figure 6 plots the waveguide modes in k-space for two

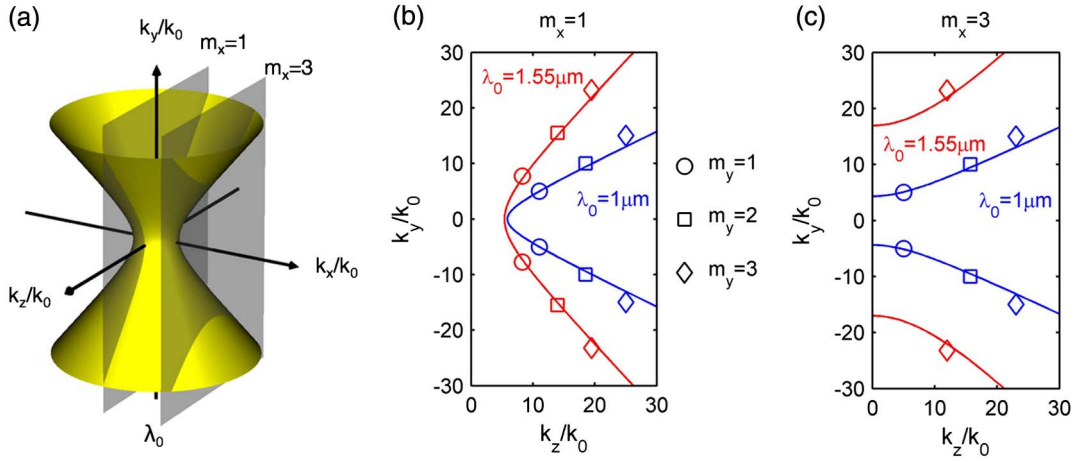

Fig. 4. (Color online) Waveguide modes plotted in k-space at different free-space wavelengths λ_0 for the waveguide with cross section of 100 by 100 nm. (a) Hyperboloid IFC of the indefinite metamaterial at the wavelength of λ_0. Two cutting planes in gray color at $k_x = 0$ and $k_x/k_0 = \lambda_0/L_x$ represent mode orders of $m_x = 1$ and $m_x = 3$, respectively. The crossing curves between the two cut planes and the hyperboloid IFC are shown in (b) and (c), respectively, at different wavelengths of $\lambda_0 = 1$ μm (blue color) and $\lambda_0 = 1.55$ μm (red color). The markers in (b) and (c) represent the $(1, m_y)$ and $(3, m_y)$ modes calculated from multilayer metamaterial waveguide structures. It is noted that the hyperbolic curves have changed their opening directions from the z direction in (b) to the y direction in (c), which will lead to the waveguide mode cutoff for the (3, 1) and (3, 2) modes at $\lambda_0 = 1.55$ μm shown in (c). Only the $k_z > 0$ part of the IFC is shown.

waveguides with the same height $L_y = 100$ nm but different widths, $L_x = 120$ nm and $L_x = 70$ nm, respectively. In Fig. 6(a), three cutting planes corresponding to $m_y = 1$, 2, and 3 for the fixed L_y are drawn in red, green, and blue, respectively. The crossing circles between the cutting planes and the hyperboloid IFC surface are plotted in Figs. 6(b) and 6(c) for differentwaveguide widths. The circular IFC in k_x-k_z plane implies that a waveguide mode will exist if k_x is less than the radius of the circle. In Fig. 6(b), the (3, 1) mode has cutoff when $L_x = 120$ nm. In Fig. 6(c), all the $(3, m_y)$ modes and the (2, 1) mode have cutoff, due to the increased k_x value as L_x gets smaller. In addition, all the $(1, m_y)$ modes are not sensitive to the change of the waveguide width, due to $k_x = 0$. According to the above analysis in Figs. 5 and 6, a metamaterial waveguide with a small width L_x and a large height L_y (equivalent to a large k_x and a small k_y) tends to have mode cutoff for high-order modes at a fixed wavelength.

As indicated by the above analysis, the deep-subwavelength waveguides made of indefinite metamaterial support ultralarge wave vector components in both the propagation direction (k_z) and the lateral direction (k_x and k_y), due to the unbounded hyperbolic dispersion. It will result in ultrahigh effective refractive indices n_{eff}, which is defined as

$$n_{\text{eff}} = \sqrt{n_{\text{eff},x}^2 + n_{\text{eff},y}^2 + n_{\text{eff},z}^2} = \sqrt{\left(\frac{k_x}{k_0}\right)^2 + \left(\frac{k_y}{k_0}\right)^2 + \left(\frac{k_z}{k_0}\right)^2}. \tag{4}$$

Figure 7(a) presents the dependence of effective refractive indices n_{eff} for the $(1, m_y)$ modes on waveguide sizes L for

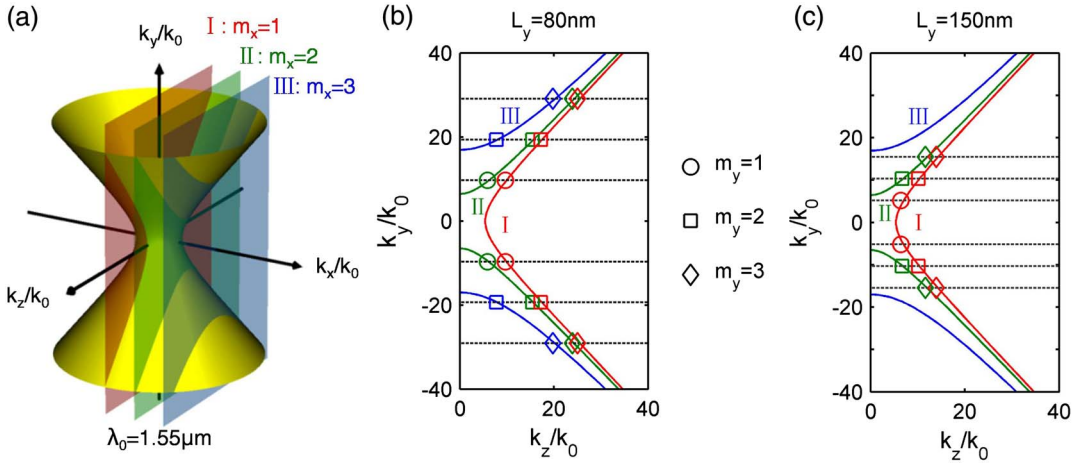

Fig. 5. (Color online) Waveguide modes plotted in k-space at different waveguide height L_y for a fixed width $L_x = 100$ nm. (a) Hyperboloid IFC of the indefinite metamaterial at $\lambda_0 = 1.55$ μm. Three cutting planes of I, II, and III represent mode orders of $m_x = 1$, $m_x = 2$, and $m_x = 3$, respectively. The three crossing curves between the cutting planes and the hyperboloid IFC are shown in (b) and (c), for different waveguide heights of $L_y = 80$ nm and $L_y = 150$ nm, respectively. The markers in (b) and (c) represent the (m_x, m_y) modes calculated from multilayer metamaterial waveguide structures. The horizontal dashed lines show the location $m_y = 1$, 2, and 3 for a certain waveguide height L_y. It is observed that k_y will decrease as L_y gets larger, which will result in the waveguide mode cutoff for high-order modes, such as the (2, 1), (3, 2), and (3, 3) modes, as shown in (c). Only the $k_z > 0$ part of the IFC is shown.

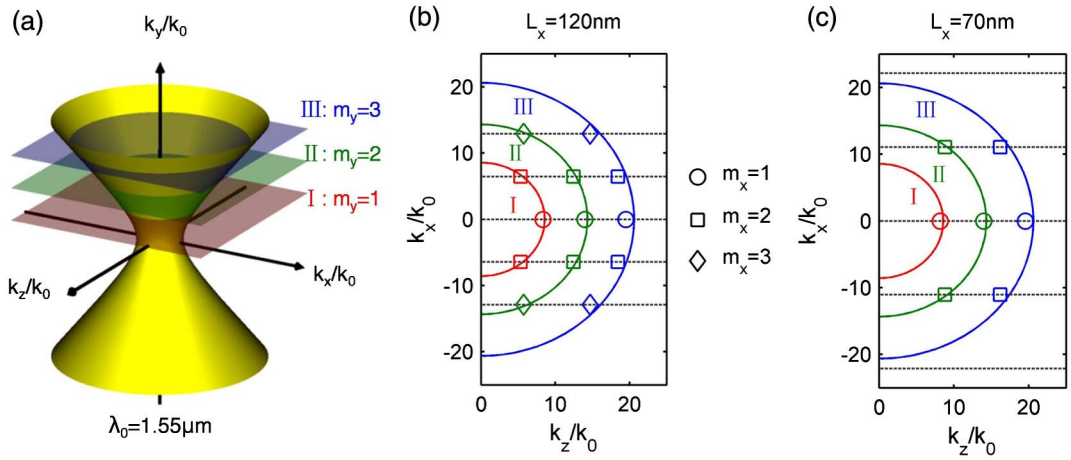

Fig. 6. (Color online) Waveguide modes plotted in k-space at different waveguide widths L_x for a fixed height $L_y = 100$ nm. (a) Hyperboloid IFC of the indefinite metamaterial at $\lambda_0 = 1.55$ μm. Three cutting planes of I, II, and III represent mode orders of $m_y = 1$, $m_y = 2$, and $m_y = 3$, respectively. The three crossing circles between the cut planes and the hyperboloid IFC are shown in (b) and (c), for different waveguide widths of $L_x =$ 120 nm and $L_x = 70$ nm, respectively. The markers in (b) and (c) represent the (m_x, m_y) modes calculated from multilayer metamaterial waveguide structures. The horizontal dashed lines show the location $m_x = 1, 2$, and 3 for a certain waveguide width L_x. It is observed that k_x will increase as L_x gets smaller, which will result in the waveguide mode cutoff for high-order modes, such as the (2, 1), (3, 2), and (3, 3) modes, as shown in (c). Only the $k_z > 0$ part of the IFC is shown.

waveguides with square cross sections ($L_x = L_y = L$) at $\lambda_0 = 1.55$ μm. The effective refractive index will increase as the waveguide size shrinks and the mode order m_y gets higher. For example, $n_{\text{eff}} = 56.6$ is obtained for the (1, 3) mode for a waveguide with $L = 50$ nm, and $n_{\text{eff}} = 62.0$ is achieved for the (1, 2) mode for a waveguide with $L = 30$ nm. For $L = 30$ nm, the (1, 3) mode is not available from the multilayer waveguide structure calculation, since the period $a(= 10$ nm) of the multilayer metamaterial structure is larger than the operation wavelength. In fact, the waveguide mode in the metal–dielectric multilayer structure is intrinsically the evolution of coupled metal–dielectric–metal (MDM) plasmonic modes [41]. For the multilayer structure with a period of 10 nm, there are only three silver layers and thus two coupled MDM plasmonic modes, so that only two modes [the (1, 1) and (1, 2) modes] are supported. The wave vectors of the waveguide modes shown in Fig. 7(a) are plotted in k-space in Fig. 7(b), which match the effective medium calculation (solid curve) in the low k region ($k \ll 2\pi/a$). In the high k region (when $L <= 50$ nm), as the wavelength is close to the period of the multilayer structure a, the nonlocal effect of the metamaterial becomes significant, so that the effective medium response of the multilayer structures deviates from the ideal effective medium theory [42], leading to reduced wave vectors in the realistic multilayer structures. It is demonstrated that ultralarge wave vectors are supported with the multilayer metamaterial waveguide structures in both y and z directions, leading to ultrahigh effective refractive indices n_{eff} in such materials.

Finally, mode propagation of the (1, 1) modes inside the metamaterial waveguides is studied in 3D real space. Figures 8(a) and 8(b) plot the distributions of magnetic field H_x for the (1, 1) modes at $\lambda_0 = 1.55$ μm in waveguides with square cross sections of 30 by 30 nm, and 50 by 50 nm, respectively. The waveguide mode properties are listed at the bottom of each figure. The tradeoff between the mode confinement

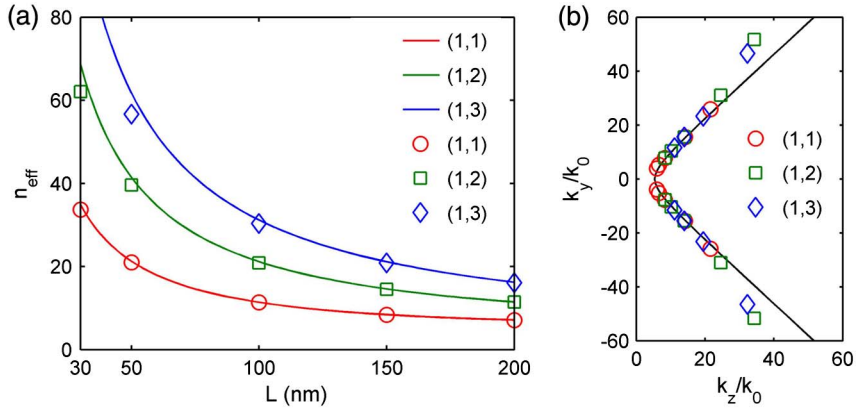

Fig. 7. (Color online) (a) Effective refractive indices n_{eff} for the $(1, m_y)$ modes as functions of waveguide sizes L for metamaterial waveguides with square cross sections at $\lambda_0 = 1.55$ μm. Solid curves are calculated from the effective medium method and markers represent the simulation results from multilayer metamaterial waveguide structures. It is shown that a smaller waveguide size L and a higher mode order m_y will lead to a larger refractive index; (b) The wave vectors of the waveguide modes shown in (a) are plotted in k-space, which match the effective medium calculation (solid curve) in the low k region ($k \ll 2\pi/a$). In the high k region (when $L \leq 50$ nm), as the wavelength is close to the period of the multilayer a, the wave vectors calculated from the multilayer structure deviate from the predication of effective medium theory due to the nonlocal effect.

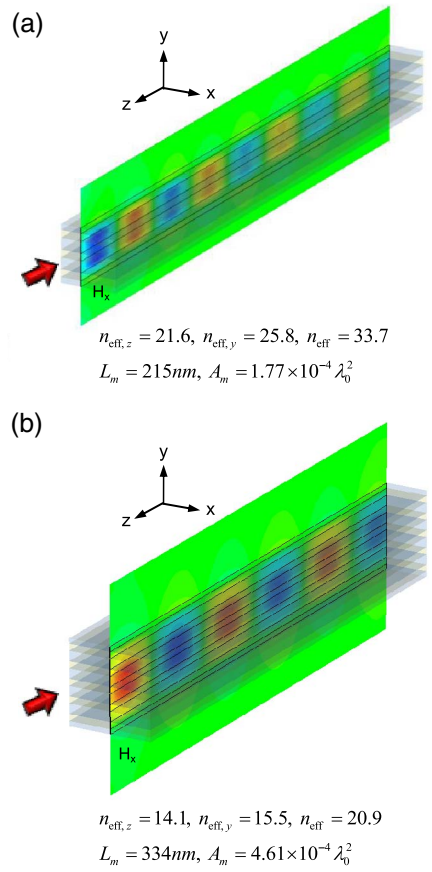

Fig. 8. (Color online) Mode propagation of the (1, 1) modes at $\lambda_0 = 1.55\ \mu$m inside the metamaterial waveguides with square cross sections of (a) 30 nm by 30 nm and (b) 50 nm by 50 nm, respectively. The distributions of the magnetic field H_x are plotted. The length of the waveguides in z direction is 300 nm for both cases. The waveguide mode properties are listed on the bottom of each figure.

and the propagation length is shown clearly, where the waveguide with $L = 30$ nm has a smaller mode area but a shorter propagation length, compared to the waveguide with $L = 50$ nm. Although the propagation length seems not quite long, the guided waves actually can undergo many oscillations before they are completely absorbed due to the ultralarge waveguide mode indices. These available oscillations are attractive for many practical applications such as nanoscale Mach–Zehnder interferometers, nanoring resonators, and nanoscale optical splitter with deep-subwavelength dimensions. A possible way to enhance the propagation length is the incorporation of gain materials, in which the optical loss can be reduced significantly by loss compensation [43,44]. Although the metamaterial waveguide is multimode, a specific mode can be selectively excited by controlling the excitation source profile. Considering that the fabrication of ultrathin 4 nm silver film is challenging (but feasible [39]), a relatively thicker silver film can be used in the metamaterial multilayers to obtain the ultrahigh refractive indices. Very promising applications such as nanolasers are expectable due to the large Purcell factor arising from the ultratight mode confinement if enough gain intensity is provided [31,45].

In conclusion, we have demonstrated nanoscale optical waveguides made of metal–dielectric multilayer indefinite metamaterials supporting ultrahigh effective refractive indices. Numerical simulation based on both metal–dielectric multilayer structures and the effective medium approach is performed systematically to analyze waveguide mode properties for different mode orders, including waveguide mode indices, propagation lengths, mode areas, and effective refractive indices. The mechanism of waveguide mode cutoff for high-order modes is revealed with IFCs in the wave vector space. The deep-subwavelength optical waveguide with size less than $\lambda_0/50$ and mode area in the order of $10^{-4}\lambda_0^2$ is realized, and an ultrahigh effective refractive index up to 62.0 is achieved at $\lambda_0 = 1.55\ \mu$m. These ultracompact metamaterial waveguides opens a new realm of the enhanced light–matter interactions for many promising applications.

ACKNOWLEDGEMENTS

This work was partially supported by the Department of Mechanical and Aerospace Engineering, the Materials Research Center, the Intelligent Systems Center, and the Energy Research and Development Center at Missouri S&T, the University of Missouri Research Board, the Ralph E. Powe Junior Faculty Enhancement Award, and the National Natural Science Foundation of China (grants 61178062 and 60990322).

REFERENCES

1. V. G. Veselago, "The electrodynamics of substances with simultaneously negative values of permittivity and permeability," Sov. Phys. Usp. **10**, 509–514 (1968).
2. J. B. Pendry, A. J. Holden, D. J. Robbins, and W. J. Stewart, "Magnetism from conductors and enhanced nonlinear phenomena," IEEE Trans. Microwave Theory Tech **47**, 2075–2084 (1999).
3. R. A. Shelby, D. R. Smith, and S. Schultz, "Experimental verification of a negative index of refraction," Science **292**, 77–79 (2001).
4. Z. Jacob, L. V. Alekseyev, and E. Narimanov, "Optical hyperlens: far-field imaging beyond the diffraction limit," Opt. Express **14**, 8247–8256 (2006).
5. A. Salandrino and N. Engheta, "Far-field subdiffraction optical microscopy using metamaterial crystals: theory and simulations," Phys. Rev. B **74**, 075103–075105 (2006).
6. Z. Liu, H. Lee, Y. Xiong, C. Sun, and X. Zhang, "Far-field optical hyperlens magnifying sub-diffraction-limited objects," Science **315**, 1686 (2007).
7. J. B. Pendry, D. Schurig, and D. R. Smith, "Controlling electromagnetic fields," Science **312**, 1780–1782 (2006).
8. D. Schurig, J. J. Mock, B. J. Justice, S. A. Cummer, J. B. Pendry, A. F. Starr, and D. R. Smith, "Metamaterial electromagnetic cloak at microwave frequencies," Science **314**, 977–980 (2006).
9. W. Cai, U. K. Chettiar, A. V. Kildishev, and V. M. Shalaev, "Optical cloaking with metamaterials," Nat Photon **1**, 224–227 (2007).
10. J. T. Shen, P. B. Catrysse, and S. Fan, "Mechanism for designing metallic metamaterials with a high index of refraction," Phys. Rev. Lett. **94**, 197401 (2005).
11. J. Shin, J.-T. Shen, and S. Fan, "Three-dimensional metamaterials with an ultrahigh effective refractive index over a broad bandwidth," Phys. Rev. Lett. **102**, 093903 (2009).
12. M. Choi, S. H. Lee, Y. Kim, S. B. Kang, J. Shin, M. H. Kwak, K.-Y. Kang, Y.-H. Lee, N. Park, and B. Min, "A terahertz metamaterial with unnaturally high refractive index," Nature **470**, 369–373 (2011).
13. D. R. Smith and D. Schurig, "Electromagnetic wave propagation in media with indefinite permittivity and permeability tensors," Phys. Rev. Lett. **90**, 077405 (2003).
14. Y. Liu, G. Bartal, and X. Zhang, "All-angle negative refraction and imaging in a bulk medium made of metallic nanowires in the visible region," Opt. Express **16**, 15439–15448 (2008).
15. J. Yao, Z. Liu, Y. Liu, Y. Wang, C. Sun, G. Bartal, A. M. Stacy, and X. Zhang, "Optical negative refraction in bulk metamaterials of nanowires," Science **321**, 930 (2008).

16. Z. Jacob, J. Y. Kim, G. Naik, A. Boltasseva, E. Narimanov, and V. Shalaev, "Engineering photonic density of states using metamaterials," Appl. Phys. B **100**, 215–218 (2010).
17. M. A. Noginov, H. Li, Y. A. Barnakov, D. Dryden, G. Nataraj, G. Zhu, C. E. Bonner, M. Mayy, Z. Jacob, and E. E. Narimanov, "Controlling spontaneous emission with metamaterials," Opt. Lett. **35**, 1863–1865 (2010).
18. T. Jiang, J. Zhao, and Y. Feng, "Stopping light by an air waveguide with anisotropic metamaterial cladding," Opt. Express **17**, 170–177 (2009).
19. Y. J. Huang, W. T. Lu, and S. Sridhar, "Nanowire waveguide made from extremely anisotropic metamaterials," Phys. Rev. A **77**, 063836 (2008).
20. W. T. Lu and S. Sridhar, "Slow light, open-cavity formation, and large longitudinal electric field on a slab waveguide made of indefinite permittivity metamaterials," Phys. Rev. A **82**, 013811 (2010).
21. Y. Cui, K. H. Fung, J. Xu, H. Ma, Y. Jin, S. He, and N. X. Fang, "Ultrabroadband light absorption by a sawtooth anisotropic metamaterial slab," Nano Lett. **12**, 1443–1447 (2012).
22. J. Yao, X. Yang, X. Yin, G. Bartal, and X. Zhang, "Three-dimensional nanometer-scale optical cavities of indefinite medium," Proc. Natl. Acad. Sci. **108**, 11327–11331 (2011).
23. X. Yang, J. Yao, J. Rho, X. Yin, and X. Zhang, "Experimental realization of three-dimensional indefinite cavities at the nanoscale with anomalous scaling laws," Nat. Photon. **6**, 450–454 (2012).
24. A. A. Govyadinov and V. A. Podolskiy, "Metamaterial photonic funnels for subdiffraction light compression and propagation," Phys. Rev. B **73**, 155108 (2006).
25. M. Yan, L. Thylén, and M. Qiu, "Layered metal-dielectric waveguide: subwavelength guidance, leveraged modulation sensitivity in mode index, and reversed mode ordering," Opt. Express **19**, 3818–3824 (2011).
26. J. Sun, J. Zhou, B. Li, and F. Kang, "Indefinite permittivity and negative refraction in natural material: graphite," Appl. Phys. Lett. **98**, 101901 (2011).
27. G.-D. Xu, T. Pan, T.-C. Zang, and J. Sun, "Characteristics of guided waves in indefinite-medium waveguides," Opt. Commun. **281**, 2819–2825 (2008).
28. F.-Y. Meng, Q. Wu, and L.-W. Li, "Transmission characteristics of wave modes in a rectangular waveguide filled with anisotropic metamaterial," Appl. Phys. A **94**, 747–753 (2009).
29. Z. Shi, G. Piredda, A. C. Liapis, M. A. Nelson, L. Novotny, and R. W. Boyd, "Surface-plasmon polaritons on metal-dielectric nanocomposite films," Opt. Lett. **34**, 3535–3537 (2009).
30. C. H. Gan and P. Lalanne, "Well-confined surface plasmon polaritons for sensing applications in the near-infrared," Opt. Lett. **35**, 610–612 (2010).
31. R. F. Oulton, V. J. Sorger, T. Zentgraf, R.-M. Ma, C. Gladden, L. Dai, G. Bartal, and X. Zhang, "Plasmon lasers at deep subwavelength scale," Nature **461**, 629–632 (2009).
32. T. M. Babinec, J. M. HausmannBirgit, M. Khan, Y. Zhang, J. R. Maze, P. R. Hemmer, and M. Loncar, "A diamond nanowire single-photon source," Nature Nanotechnol. **5**, 195–199 (2010).
33. Q. Lin, O. J. Painter, and G. P. Agrawal, "Nonlinear optical phenomena in silicon waveguides: modeling and applications," Opt. Express **15**, 16604–16644 (2007).
34. X. Yang, Y. Liu, R. F. Oulton, X. Yin, and X. Zhang, "Optical forces in hybrid plasmonic waveguides," Nano Lett. **11**, 321–328 (2011).
35. S. Han, Y. Xiong, D. Genov, Z. Liu, G. Bartal, and X. Zhang, "Ray optics at a deep-subwavelength scale: a transformation optics approach," Nano Lett. **8**, 4243–4247 (2008).
36. C. A. Foss, G. L. Hornyak, J. A. Stockert, and C. R. Martin, "Template-synthesized nanoscopic gold Particles: optical spectra and the effects of particle size and shape," J. Phys. Chem. **98**, 2963–2971 (1994).
37. A. Sihvola, *Electromagnetic Mixing Formulas and Applications* (Institution of Electrical Engineers, 1999).
38. P. B. Johnson and R. W. Christy, "Optical constants of the noble metals," Phys. Rev. B **6**, 4370–4379 (1972).
39. W. Chen, M. D. Thoreson, S. Ishii, A. V. Kildishev, and V. M. Shalaev, "Ultra-thin ultra-smooth and low-loss silver films on a germanium wetting layer," Opt. Express **18**, 5124–5134 (2010).
40. A. Chandran, E. S. Barnard, J. S. White, and M. L. Brongersma, "Metal-dielectric-metal surface plasmon-polariton resonators," Phys. Rev. B **85**, 085416 (2012).
41. J. Elser, A. A. Govyadinov, I. Avrutsky, I. Salakhutdinov, and V. A. Podolskiy, "Plasmonic nanolayer composites: coupled plasmon polaritons, effective-medium response, and subdiffraction light manipulation," J. Nanomater. **2007**, 79469 (2007).
42. J. Elser, V. A. Podolskiy, I. Salakhutdinov, and I. Avrutsky, "Nonlocal effects in effective-medium response of nanolayered metamaterials," Appl. Phys. Lett. **90**, 191109 (2007).
43. S. Xiao, V. P. Drachev, A. V. Kildishev, X. Ni, U. K. Chettiar, H.-K. Yuan, and V. M. Shalaev, "Loss-free and active optical negative-index metamaterials," Nature **466**, 735–738 (2010).
44. X. Ni, S. Ishii, M. D. Thoreson, V. M. Shalaev, S. Han, S. Lee, and A. V. Kildishev, "Gain-assisted hyperbolic metamaterials," in *Quantum Electronics and Laser Science Conference (QELS)*, OSA Technical Digest (Optical Society of America, 2012), paper QTu1G.
45. M. A. Noginov, G. Zhu, A. M. Belgrave, R. Bakker, V. M. Shalaev, E. E. Narimanov, S. Stout, E. Herz, T. Suteewong, and U. Wiesner, "Demonstration of a spaser-based nanolaser," Nature **460**, 1110–1112 (2009).